Available online at www.sciencedirect.com
SCIENCE DIRECT®
Advances in Space Research 37 (2006) 483–493
ADVANCES IN SPACE RESEARCH (a COSPAR publication)
www.elsevier.com/locate/asr

Electron cyclotron microinstability in the foot of a perpendicular shock: A self-consistent PIC simulation

L. Muschietti [a,*], B. Lembège [b]

[a] Space Sciences Lab., University of California, Berkeley, CA 94720, USA
[b] CETP-CNRS-UVSQ, Velizy, F-78140, France

Received 28 September 2004; received in revised form 31 January 2005; accepted 23 March 2005

Abstract

We have performed one-dimensional full particle simulations of perpendicular shocks and found that an electron cyclotron microinstability can develop in the foot during the self-reformation phase of low β_i supercritical shocks. The instability is excited by the beam of reflected ions interacting with the incoming electrons. It exhibits a rapid growth, and propagates along the shock normal towards upstream. This instability, which does not require high Mach number, has a frequency comparable to the electron cyclotron frequency and a wavelength shorter than the electron inertia length. It basically results from the coupling of electron Bernstein waves with an ion beam mode carried by the reflected ions. Dispersion properties in the foot are analysed. We discuss the effects of varying parameters, in particular as the fake ion-to-electron mass ratio used in the simulations converges to more realistic values. Comparison with other microinstabilities evidenced in recent full particle simulations of shocks is outlined.

Keywords: Collisionless shocks; Plasma microinstabilities; Shock foot; Numerical simulation; Electron cyclotron

1. Introduction

It has been surmised for many years that the presence of a beam of reflected ions in the foot of a supercritical shock could trigger plasma microinstabilities. The proposition still holds interest considering the continuing search for dissipation mechanisms in collisionless shocks. A lot of past works, dating as far back as the 70's, modelled the foot as a three-population plasma made of the incoming ions, the reflected ions, and the electrons. Possible instabilities associated with relative drifts between the populations were analysed, mostly through studies of the dispersion relation. A review of those efforts may be found in Wu et al. (1984). Although they provide useful insights into potential instabilities, those works were limited in that they considered the foot as a stationary, homogeneous plasma independent from the whole shock structure and then investigated its properties with chosen ad hoc parameters. Yet we know from full particle simulations that the foot is an evolving and transient feature, which forms and disappears during the cycle of shock front self-reformation, even at moderate yet supercritical Mach numbers (Biskamp and Welter, 1972; Lembège and Dawson, 1987; Lembège and Savoini, 1992; Scholer et al., 2003).

Only recently, thanks to advances in computational power, has it been possible to design and run particle-in-cell (PIC) simulations of shocks with enough resolution, both spatial and temporal, to enable one to actually "see" some of the microinstabilities at work in the foot. Investigations that adopt this self-consistent approach are still few at the present time and reported in just a handful of articles. Scholer et al. (2003) set up simulations of quasi-perpendicular shocks and observe

* Corresponding author. Tel.: +1 510 643 9125; fax: +1 510 643 8302.
E-mail address: laurent@ssl.berkeley.edu (L. Muschietti).

0273-1177/$30
doi:10.1016/j.asr.2005.03.077

the modified two-stream instability. This instability (MTSI) is driven by a relative drift U_{e-i} between electrons and ions across the ambient magnetic field **B** (McBride et al., 1972; McBride and Ott, 1972; Matsukiyo and Scholer, 2003). It has the remarkable property to operate for moderate drifts $U_{e-i} < v_{te}$, where v_{te} is the electron thermal speed, even with $T_e \sim T_i$. The unstable frequency lies between the ion and electron gyrofrequencies, so that the ions are assumed unmagnetized yet the electrons strongly magnetized. In the electrostatic limit of the dispersion relation, the electron term associated with their free motion along **B** looks as $(\omega_e/\omega)^2(\cos\theta)^2$, where ω_e is the electron plasma frequency and θ is the wave propagation angle to **B**. This term provides the second "stream", the first one being the unmagnetized ion term $(\omega_i/\omega)^2$ with ω_i the ion plasma frequency. At very oblique angles such that $\cos\theta \sim \sqrt{m/M}$ the electrons have an effective mass comparable to the ions, which gives rise to a two-stream-like instability, hence the name MTSI. On the other hand, in a strictly perpendicular geometry the second "stream" vanishes and the instability disappears.

A perpendicular shock has the appeal of simple macroscopic conditions. Because of the geometry, there is only one component of the magnetic field to consider, $B_z(x,t)$, where $\hat{z}$ points to the direction of the upstream magnetostatic field **B** and x measures the distance along the shock normal. A single parameter links downstream (subscript 2) and upstream (subscript 1) values of the flow velocities, densities, and magnetic field amplitudes: $V_1/V_2 = N_2/N_1 = B_{z2}/B_{z1} = r$ (e.g., Tidman and Krall, 1971, Ch.1). The shock exhibits no upstream dispersive effects. Moreover, all the forces acting on the particles are in the plane $[x,y]$, making their dynamical motion effectively two-dimensional.

PIC simulations of perpendicular shocks with good resolution have also recently been reported (Shimada and Hoshino, 2000; Hoshino and Shimada, 2002). These authors investigated shocks with a high Alfven Mach number M_A, in the foot of which a Buneman instability takes place between incoming electrons and the reflected ion population. This leads to the formation of electron holes in phase space and, according to these authors, to the subsequent acceleration of some electrons to high energies through shock surfing. The simulation runs were performed with a ratio of plasma frequency to cyclotron frequency $\omega_e/\Omega_e = 20$. The value is quite large compared to values commonly used in full particle simulations of shocks, for example $\omega_e/\Omega_e = 2$ in Hada et al. (2003) and some runs of Scholer et al. (2003). This important parameter affects the simulations and is linked to the ratio between electron inertia length λ_e and Debye length λ_d through the electron beta,

$$\lambda_e/\lambda_d = (2/\beta_e)^{1/2}(\omega_e/\Omega_e). \quad (1)$$

In their runs, Shimada and Hoshino (2000) use $\beta_e = 0.15$ and have the electron inertia length about 70 times the Debye length, which leaves plenty of room for electrostatic waves to develop. However, the authors utilize such a small ion-to-electron mass ratio, $M/m = 20$, that their results are controversial. Indeed, as the mass ratio increases toward realistic values, the electron thermal speed $v_{te} = (T_e/m)^{1/2}$ becomes an ever larger multiple of the Alfven velocity V_A since

$$v_{te}/V_A = (\beta_e/2)^{1/2}(M/m)^{1/2}. \quad (2)$$

Hence, to prevent the electrons from overlapping in phase space with the reflected ions, whose velocity is proportional to $M_A V_A$, shocks with large M_A producing large relative drifts U_{ri-e} between the reflected ions ('ri') and the electrons ('e') need be considered. In order to satisfy the Buneman condition that $U_{ri-e} > \sqrt{2}v_{te}$, ever higher Mach numbers are required as the mass ratio approaches more realistic values. Scholer and Matsukiyo (2004) carried out simulations with a fixed, moderate Mach number ($M_A = 4.5$) and quasi-perpendicular geometry ($\theta = 87°$), yet increasing mass ratios. They show the Buneman instability to be stabilized at higher ratios.

As we will demonstrate in this paper, there is a microinstability in the foot of perpendicular shocks which does not require a large U_{ri-e}. The instability basically results from the coupling of electron Bernstein waves with an ion beam mode carried by the reflected ions. Its phase velocity can lie within the distribution of electrons, which makes the instability kinetic as opposed to the fluid Buneman instability. It has a short wavelength, under an electron inertia length, and is mostly electrostatic.

2. Simulation conditions

2.1. Darwin PIC code

A newly developed one-dimensional code is used for the simulations. It follows the motions of both ion and electron macroparticles, as a standard full particle PIC code, yet implements the Darwin model for computing the evolving electromagnetic fields. The Darwin model (e.g. Hewett, 1985) has equations very similar to the exact Maxwell equations. Faraday's law is included for example. The Darwin equations, though, neglect the transverse part of the displacement current, which eliminates radiation. This affords us a larger time step than the Courant condition would otherwise impose on a grid resolving the Debye length. In a "Maxwell" electromagnetic code, the time step dt is bounded by the Courant condition applied to the propagation of radiation over the grid at speed c. Thus, the large number of steps required to reach an ion cyclotron period is given by

$$N_t > (2\pi\lambda_d/\delta)(c/v_{te})(\omega_e/\Omega_e)(M/m), \quad (3)$$

where δ is the size of a grid cell. It is well known that simulationists play with the mass ratio in order to reduce the computational effort. Less known is that they compromise also with using too small a c/v_{te} ratio. This ratio yet, besides entering into Eq. (3), determines a compression of the spatial scales between the electron inertia length λ_e and the much smaller electron Debye length λ_d. By adopting a Darwin model we drop the factor c/v_{te} from the right-hand side of Eq. (3). We at once reduce the required number of steps to reach an ion cyclotron period and are freer to better separate λ_d from λ_e, which makes this code quite attractive for the problem of concern.

2.2. Initialization

Our PIC code is open-boundary and the method for producing the shock is similar to that used by Leroy et al. (1982). Incident on the left boundary are the upstream ions and electrons while exiting on the right boundary are heated particles. In between, the simulation box contains the shock transition, which is at rest in average. In other words, we work in the so-called shock frame of theoretical studies (Tidman and Krall, 1971). Our shock frame is also the so-called normal incidence frame where the upstream velocity is parallel to the shock normal. While preparing a simulation run, we use fluid theory and general flux conservation equations in order to establish a specific model for the macroscopic transition layer between the upstream and the downstream plasmas compatible with Rankine–Hugoniot. Profiles for quantities such as electron and ion densities $N_e(x)$, $N_i(x)$, bulk velocity flows $V_{ex}(x)$, $V_{ix}(x)$, $V_{ey}(x)$, etc. are used in the code to initiate the simulations and define the boundary conditions. In practice, we load the particles with the appropriate drift, velocity spread, and number density, and the fields automatically come out. After many steps, once the population of reflected ions has built up, a completely self-consistent shock structure emerges. For somewhat large β_i it evolves into a quasi-steady structure, while for small β_i as here ($\beta_i = 0.022$) one observes the self-reformation of the shock front . More details about the simulation conditions and the code will be published elsewhere.

For the main run reported here, the simulation box consists of 1500 grid cells, each with an average of 1000 macroparticles per species. The cell size is $\delta = 1.87\lambda_{d,1}$ with $\lambda_{d,1}$ the upstream electron Debye length. The timestep is $dt = 0.2\bar{\omega}_p^{-1}$, where $\bar{\omega}_p$ is the electron plasma frequency averaged over the box. Subsequently, time is given in units of $\bar{\omega}_p^{-1}$, velocity in units of the upstream electron thermal speed $v_t \equiv v_{te,1}$, and distance in units of $v_t/\bar{\omega}_p$. In plots, however, distances are shown in electron inertia length $\lambda_e = c/\bar{\omega}_p$. Also, magnetic field and density are shown in units of their upstream values B_1 and N_1. We simulate a supercritical shock with an Alfven Mach number $M_A = 3.0$. The ion-to-electron mass ratio $M/m = 100$ and the temperature ratio $T_e/T_i = 1.56$. The upstream values of the electron plasma frequency and gyrofrequency are $\omega_{e,1} = 0.624\bar{\omega}_p$ and $\Omega_{e,1} = 0.315\bar{\omega}_p$, respectively. Detailed physical parameters for each species are given in Table 1. The choice of parameters is quite close to that in Hada et al. (2003), save for the grid resolution which is 2.7 times better and the particle statistics which is an order of magnitude larger herein.

2.3. Frame transformation, characteristic velocities, and specular reflection

To avoid confusion when discussing results about shocks, it is important to know in which frame velocities are measured. Two inertial frames are popular in numerical studies: the upstream and the downstream frames, where the usptream, respectively downstream, plasma is at rest. Due to the reformation process, the shock front itself is highly nonstationary and cannot provide an inertial frame. However, there is an average shock frame in between the upstream and the downstream frames, which is inertial. This frame has the upstream plasma impinging from the left with a positive velocity V_1 that determines the shock Mach number, $V_1 = V_A M_A$. It has the downstream plasma leaving to the right with a positive velocity V_2. The velocities V_2 and V_1 are related by the compression ratio r, which in a perpendicular geometry controls both density and magnetic compression: $r = N_2/N_1 = V_1/V_2 = B_2/B_1 > 1$. This paper, unless specified otherwise, uses the average shock frame.

During the cyclic self-reformation of the shock, the front's position moves toward downstream and then jumps back upstream where the new front forms. The front's speed is thus unsteady, which makes it a priori difficult to apply the concept of specular reflection of the incoming ions at the front. However, our simulations as well as the results of Lee et al. (2004), who discuss this question in detail, show that the front's speed is

Table 1
Upstream plasma parameters for each species

Name	Electrons	Ions
Plasma frequency	$\omega_e = 0.624$	$\omega_i = 0.0624$
Gyrofrequency	$\Omega_e = 0.315$	$\Omega_i = 3.15 \times 10^{-3}$
Thermal velocity	$v_{te} = 1$	$v_{ti} = 8.0 \times 10^{-2}$
Debye length	$v_{te}/\omega_e = 1.60$	$v_{ti}/\omega_i = 1.28$
Inertial length	$c/\omega_e = 24$	$c/\omega_i = 240$
Gyroradius	$\rho_e = 3.17$	$\rho_i = 25.4$
Beta	$\beta_e = 0.035$	$\beta_i = 0.022$
Cyclotron period	$\tau_{ce} = 20$	$\tau_{ci} = 2.0 \times 10^3$

close to the downstream velocity V_2 at times of maximum particle reflection. For the sake of simplicity we will thus assume that the incident ions impinges on the front with a bulk velocity

$$U_1 = V_1 - V_2 = V_1(1 - 1/r) \tag{4}$$

which after specular reflection becomes $U_r = -U_1$. As approximate as it may be, this picture is in fact borne out by, e.g., Fig. 2 of Lee et al. (2004), or Fig. 4 of Scholer and Matsukiyo (2004), which both display the ion phase space in the downstream frame. One can see that the reflected speed is the minus of the injected speed. As measured in the average shock frame, we will therefore assess the reflected velocity to be

$$V_{ri} = -V_1(1 - 2/r) \tag{5}$$

The velocity is negative since these ions are moving back from the shock ramp toward upstream. In our simulations $r \approx 3$, hence the reflected velocity is predicted to be about $-1/3V_1$. If one further assumes that the electrons in the foot adapt their velocity so as to maintain a zero normal current, their bulk speed in the foot can be expressed in terms of the ion reflection rate α and the incident ion speed:

$$V_e = V_1(1 - 2\alpha + 2\alpha/r). \tag{6}$$

There are thus two possible types of instability within the foot: one associated with the relative drift $U_{i-e} \equiv V_i - V_e$ between the incoming ions and the electrons, and one associated with the relative drift $U_{ri-e} \equiv V_{ri} - V_e$ between the reflected ions and the electrons. For shock simulations which use the piston method and hence have the upstream plasma at rest, their velocities $\tilde{V}$ are related to the velocities here by $\tilde{V} = V - V_1$ where V_1 is the velocity at which the shock sweeps through the upstream plasma (i.e., the shock velocity $V_{sh} = M_A V_A$). We will return to these expressions in Section 4 where the dispersive properties of the instability we observe are analysed.

3. Simulation results

Fig. 1 shows the process of shock self-reformation. In the top panel, profiles of the magnetic field B_z are stacked in time. The horizontal axis indicates distance along the shock normal in units of electron inertia length λ_e. Time runs from bottom to top and is marked on the vertical axis at the left in units of inverse electron plasma frequency. For displaying purposes, the successive profiles have been shifted both vertically and horizontally by an amount indicated via the oblique line on the left. The line shows the position of a point that stays at rest in the simulation frame. In other words, the last profile at $t = 1440$ is shifted by nearly $45\lambda_e$ as compared with the first profile at $t = 120$. On the vertical axis at the right, we provide a scale for the profiles' amplitude. Note the sharp magnetic ramp with a characteristic width of a few λ_e, which reappears periodically. Note also the foot which develops in front of the ramp to eventually turn into a new shock front with a new sharp ramp. The process repeats itself periodically, which yields a reformation time $T_{ref} \approx 540\bar{\omega}_p^{-1}$. We will return below to this evaluation while discussing Fig. 4. The bottom panel of Fig. 1 displays the electron density profiles associated with the magnetic profiles of the top panel. Conspicuous is a short-wavelength microinstability which emerges in the region of the foot whenever the latter builds up. A display of the ion density (not shown here) reveals the same features as N_e, yet with some minor amplitude differences.

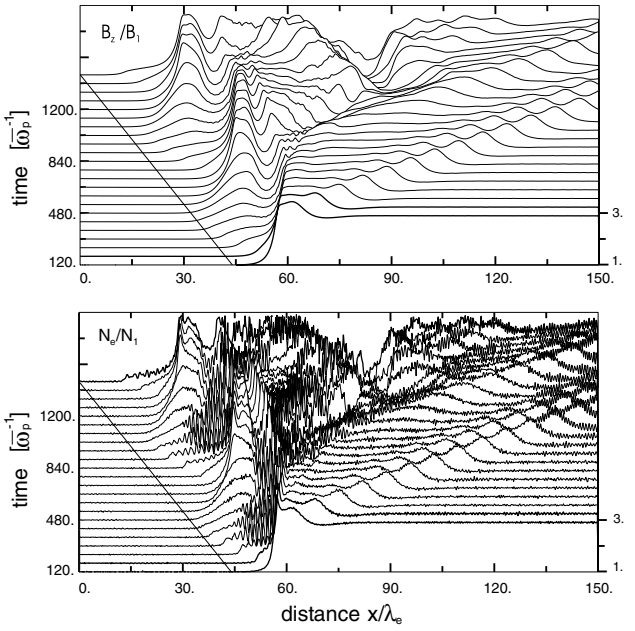

Fig. 1. Top: profiles of magnetic field B_z stacked in time. Horizontal axis shows distance along the shock normal in electron inertia length λ_e. Time runs from bottom to top and is marked on the left (units: electron plasma frequency averaged over the box, $\bar{\omega}_p$). The plot illustrates the process of shock front self-reformation. Bottom: associated profiles of electron density N_e. A short-wavelength instability reappears periodically in the foot ahead of the sharp ramp. More details in the text.

We focus now on one reformation cycle and examine the development of the microinstability in the foot. Fig. 2 shows the profiles of the magnetic field and the electrostatic field for four successive times starting at $t = 840$. The instability emerges in the foot, $x/\lambda_e \sim 60$, in front of the steep magnetic ramp. It shows up as short-scale wiggles in the profile of the electrostatic field, yet is virtually invisible in the magnetic profile. Note that they appear to develop within the flat portion of the magnetic foot, while it is slowly convected toward the right (in the simulation frame). The growth time of the instability is of order $60\bar{\omega}_p^{-1}$, i.e., $\sim 30\Omega_e^{-1}$ in terms of local electron cyclotron time. By $t = 1020$

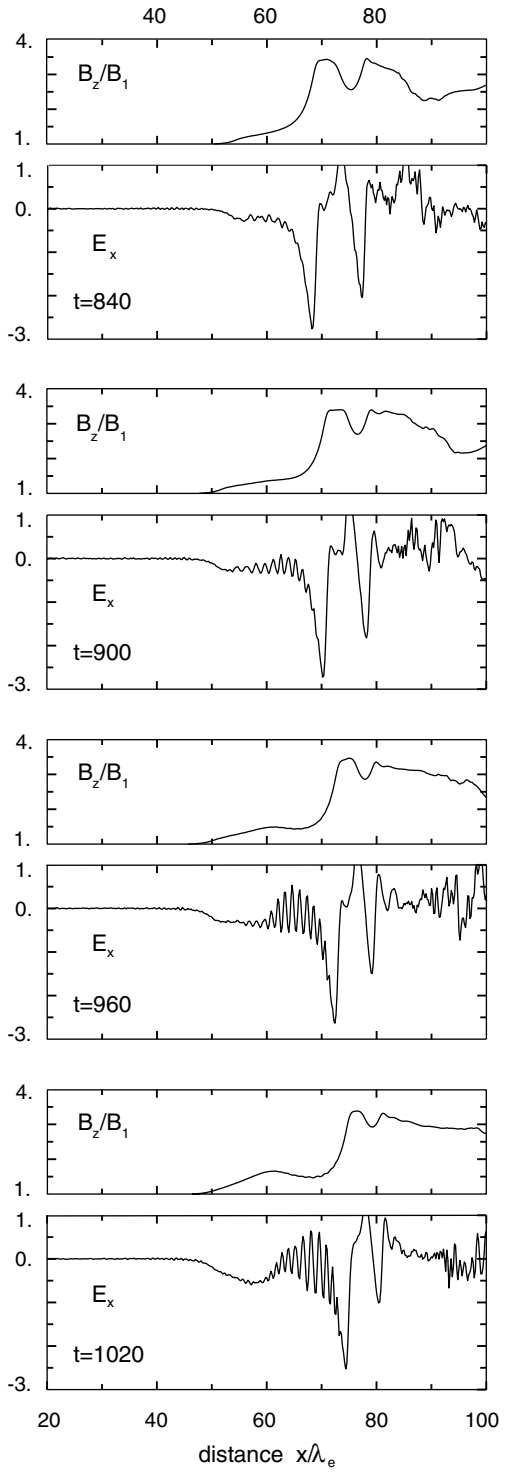

Fig. 2. Profiles of magnetic field B_z and electrostatic field E_x at four times starting from $t = 840$. B_z is normalized to its upstream value B_1 and E_x is in units of $(4\pi N m v_t^2)^{1/2}$. Note the electrostatic instability developing in front of the steep magnetic ramp ($60 < x/\lambda_e < 70$ at $t = 960$).

when a bump in the B_z profile begins to form where the new shock front will be, the unstable wave appears confined to $60 < x/\lambda_e < 72$. The reason for this spatial confinement becomes clear later.

Fig. 3 is a composite snapshot which displays details about both the field quantities and the particle phase space at time $t = 960$ when the microinstability is well developed. From top to bottom, we show the magnetic field and the density, the electrostatic field E_x, the electrostatic potential, and the electron and ion phase space $[x, v_x]$. One can see the short-wavelength wave in the density and the electrostatic field profiles, yet barely in the potential. The wavelength is equal to $15\lambda_{d,1}$ with $\lambda_{d,1}$ the upstream electron Debye length. The density compression associated with the instability is well visible in both the profile of N_e and the striations which mark the electron phase space for $60 < x/\lambda_e < 70$. Unlike the incoming ions, the reflected ions are clearly affected by the wave, which slows them down. Note the small tines that the reflected population develops at the location of the wave.

Snapshots of the ion $[x, v_x]$ phase space at various times are displayed in Fig. 4. They show the evolution of the reflected ions, from an early time at $t = 840$ when the wave is just beginning to grow to a later time at $t = 1140$ when the ions nearly close the "vortex" to be reaccelerated in the positive x-direction before penetrating the downstream region. As is well known from previous simulation works, the reflected ions are accelerated in the y-direction by the transverse component of the electric field E_y (known also as the motional electric field) until they acquire a large v_y component. They then feel a strong magnetic force $v_y B_z$ which turns their velocity around with a positive v_x component.

As for the effect of the microinstability on the reflected ion beam, an examination of Fig. 4 reveals that it spreads the particles over phase space. Unlike the first half of the "vortex" ($72 < x/\lambda_e < 77$ at $t = 1140$) which keeps almost intact its shape, the second half is strongly affected by the instability which leads to a marked scattering ($57 < x/\lambda_e < 72$ at $t = 1140$). This second half corresponds to the location where the instability reaches its maximum amplitude: time $t = 1020$ in Figs. 2 and 4. By this time the v_x component of the reflected ions that have reached beyond $x \lesssim 60$ has changed to $v_x \lesssim 0$. The relative drift U_{ri-e} between reflected ions and electrons has changed significantly, so that the resonance condition for the instability is no more satisfied. This explains the apparent confinement of the instability to the flat portion of the magnetic profile, which we noted in Figs. 2 and 3. Compare the two $t = 1020$ snapshots of Figs. 2 and 4.

Although the microinstability has a definite but limited impact on the electrons, as Fig. 3 makes clear, it has a non-negligible impact on the shock front dynamics itself via the reflected ions. These ions are strongly scattered by the instability in the second half of the vortex pattern, as noted above. Thus, reflected ions accumulate over a broad spatial extent upstream of the ramp, including (i) ions near the ramp and (ii) ions further

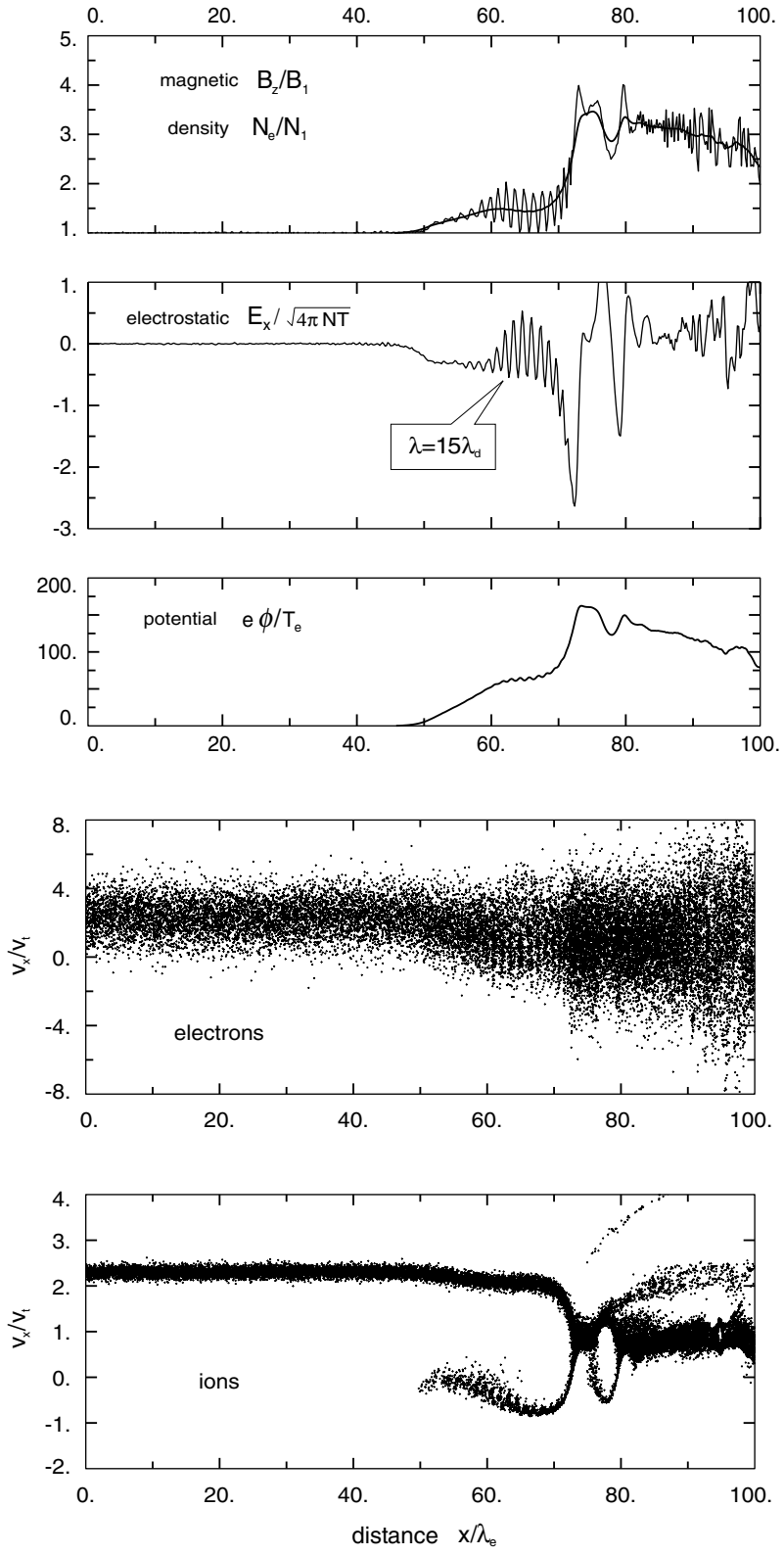

Fig. 3. Composite snapshot of field quantities and particle phase spaces at $t = 960$ when the instability is well developed. From top to bottom: magnetic field B_z (smooth line) and electron density N_e (wiggly line), electrostatic field E_x, electrostatic potential ϕ, electron and ion phase space $[x, v_x]$. Velocities are normalized to the upstream electron thermal velocity: $v_t \equiv v_{te,1}$. The instability, which is driven by the reflected ions, shows up in every quantity save for B_z (see top panel) and the incoming ions (see bottom panel).

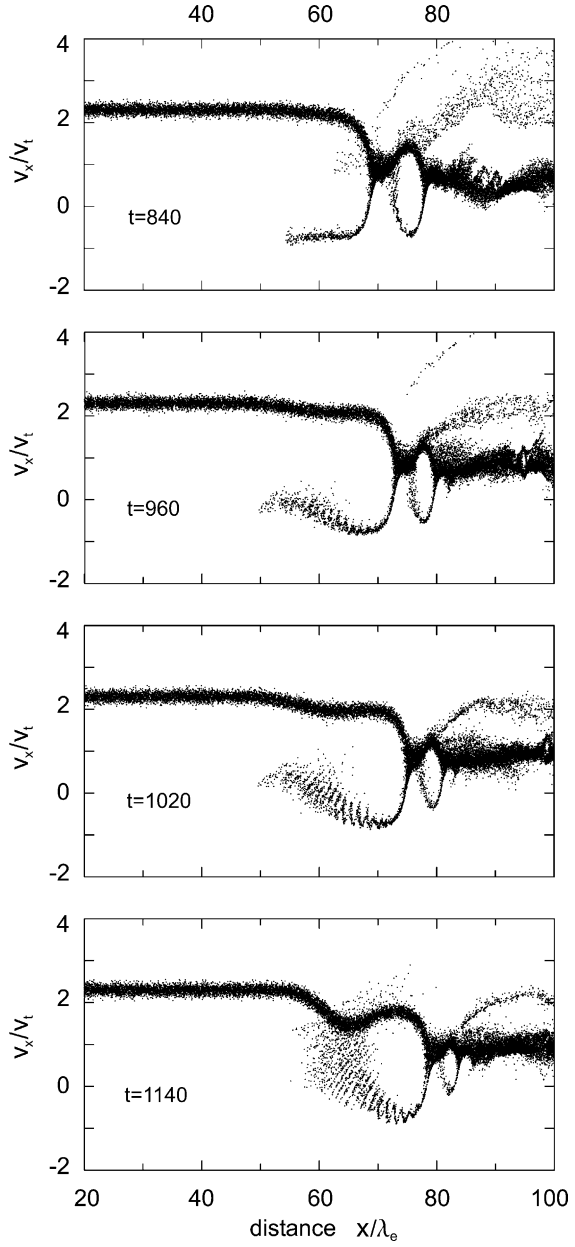

Fig. 4. Successive snapshots of ion phase space $[x, v_x]$ starting at $t = 840$ when the instability has not yet developed. Velocities are normalized to $v_t \equiv v_{te,1}$. Note how the instability affects the second half of the forming "vortex". More details in the text.

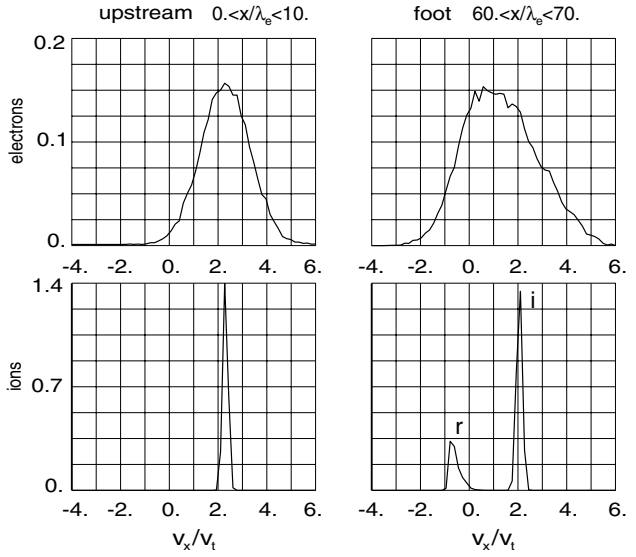

Fig. 5. Local distribution functions of electrons and ions for two positions in the simulation box at $t = 960$. Velocities are normalized to $v_t \equiv v_{te,1}$. In the lower right panel the beams of reflected and incoming ions are marked with 'r' and 'i', respectively.

from the ramp. Part (i) corresponds to ions having a shorter gyromotion and contributes to speeding up the build up of the foot near the ramp. Part (ii) has an opposite effect and contributes to the upstream end of the foot. The simulation results show that part (i) has a dominant effect and contributes to reducing the period of cyclic self-reformation. Without the presence of any microinstability, the period is comparable to the ion gyroperiod calculated from the mean downstream value of the magnetic overshoot (Lembège and Savoini, 1992), namely $\tau_{ci} = 665\bar{\omega}_p^{-1}$ for our magnetic field profile. In the present case, with the instability operating, the period is $T_{ref} \approx 540\bar{\omega}_p^{-1}$, namely 20% less than $665\bar{\omega}_p^{-1}$. The present case stands in contrast with the situation where reflected ions form a very collimated beam (without scattering) during their gyromotion and accumulate further from the ramp's location (Lembège and Dawson, 1987; Hada et al., 2003). The time necessary for the ions to describe this narrow ring in velocity space is larger than the time covered by ions of part (i). Accordingly, the build up of the foot in the present case requires a smaller time, which decreases the self-reformation period.

In order to study the possible streaming instabilities and carry out the dispersion analysis of Section 4, we have produced local distribution functions of both electrons and ions at time $t = 960$. Fig. 5 shows such distributions. For comparison purposes, they have been recorded in two different bins. Upstream distributions are measured in the interval $0 < x/\lambda_e < 10$, hence corresponds to the injected plasma. Foot distributions are taken in the interval $60 < x/\lambda_e < 70$. Note the excellent statistics in the electrons and the two beams in the ions, incoming and reflected.

4. Dispersion analysis

The observed microinstability is mostly electrostatic and grows in the flat portion of the foot. It is resonant with both the reflected ions and the broad distribution of electrons. We believe that it is a variety of the electron cyclotron drift instability, which was studied in the 70's and has since been all but forgotten (e.g. Forslund et al.,

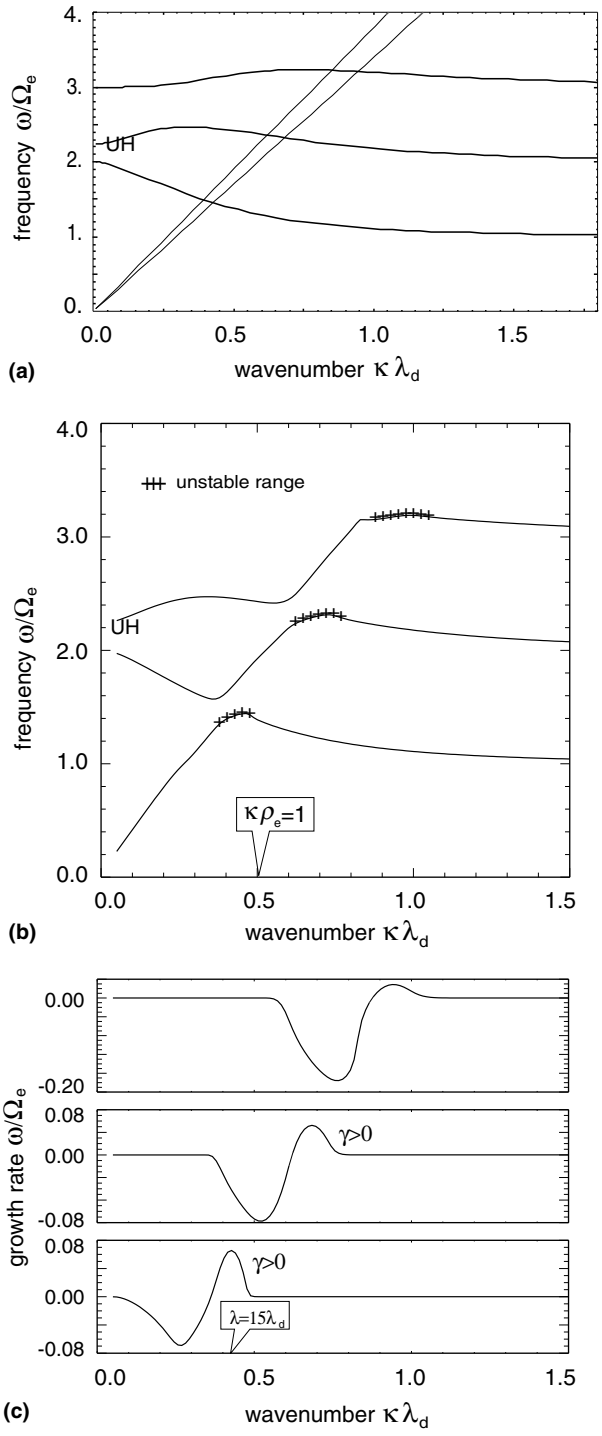

Fig. 6. Dispersion analysis of the instability. (a) Two ion beam modes (diagonal lines) intersect with the first three branches of electron Bernstein modes (thick lines) raising the possibility of coupling. Upper hybrid frequency is denoted by 'UH'. (b) Numerical solution of Eqs. (7)–(9) showing the coupling of the Bernstein waves with the slow beam mode and the associated unstable ranges. (c) Actual growth/damping rate for the three branches. More details in the text.

1970). The idea is illustrated in Fig. 6(a) which displays the two ion beam modes at $\omega = k(V_d \pm v_{ti})$ intersecting with the first three branches of Bernstein modes. At the intersections, the otherwise purely real cyclotron waves couple with the slow beam mode and acquire a positive growth driven by the positive slope of the ion beam distribution.

We suppose that the standard assumptions of an infinite, uniform plasma apply to the flat portion of the foot, and adopt a coordinate system in which the electrons are at rest, the ion beam drifts in the positive x-direction, while **B** points in the z-direction. The electrostatic dispersion reads

$$1 + \chi_e + \chi_i = 0, \tag{7}$$

where χ_e and χ_i are the susceptibilities contributed by the electrons and the ions, respectively. The electron contribution is the term for electron cyclotron Bernstein waves

$$\chi_e = -\frac{1}{k^2\lambda_d^2}\left[-1 + I_0(\eta)e^{-\eta} + 2\sum_{n=1}^{\infty} I_n(\eta)e^{-\eta}\frac{\omega^2}{\omega^2 - n^2\Omega_e^2}\right], \tag{8}$$

where $\eta \equiv (k\rho_e)^2 = (\omega_e/\Omega_e)^2(k\lambda_d)^2$. The ions are taken as unmagnetized since the duration of the foot is much less than an upstream ion gyro-period and the instability growth is seen to occur on a rapid time scale

$$\chi_i = -\frac{\alpha}{k^2\lambda_d^2}\frac{T_e}{2T_i}Z'\left(\frac{\omega - kV_{dri}}{\sqrt{2}kv_{ti}}\right) - (1-\alpha)\left(\frac{\omega_i}{\omega + kV_{di}}\right)^2. \tag{9}$$

The first term represents the reflected ion population with drift V_{dri} and relative density α. The second term, which represents the incoming ions with drift $-V_{di}$, is non-resonant and negligible for the parameters of the simulation.

A numerical solution of the dispersion relation with Eqs. (8) and (9) is displayed in Fig. 6(b). The panel displays the real part of the frequency for three simultaneous branches. The unstable ranges, which are marked with plusses, show the signature of the beam in their alignment. For $k\lambda_d \approx 0.4$ the slow beam mode couples with the first Bernstein harmonic. Similarly, there is a coupling with the second harmonic at $k\lambda_d \approx 0.7$. To draw the plot we have chosen parameters that emulate the simulation: $\omega_e/\Omega_e = 2$, $V_{dri}/v_{te} = 1.8$, $M/m = 100$, $\alpha = 0.25$, and $T_e = T_i$.

The growth rates for the three branches are indicated in the three panels of Fig. 6(c). They are seen to decrease with increasing harmonics. A rate $\gamma = 0.06\Omega_e$ is fast enough to explain the simulations, where the instability is seen to grow with a time scale of $\sim 30\Omega_e^{-1}$ (see Fig. 2). Due to the grid resolution used herein, we observe only the instability at the first harmonic. In fact the wavelength $\lambda = 15\lambda_{d,1}$, which was estimated from Fig. 3, falls right in the middle of the first unstable range. What about the associated frequency $\omega = 1.4\Omega_e$? Is that what we see?

By means of a probe we have measured the apparent frequency in the frame of the simulation box. This frequency is $0.2\omega_{e,1}$. Doppler-shifting it into the electron frame we have $\omega = 0.2\omega_{e,1} + k\,V_e$. Now, while the wavenumber is well defined, $kv_t = (2\pi/15)\omega_{e,1}$, V_e is more difficult to evaluate precisely. One can either use $F_e(v)$ shown in Fig. 5 and compute the first moment, or use Eq. (6) of Section 2.3. The former way produces $V_e = 1.3v_t$ while the latter yields $V_e = 1.5v_t$ (with $\alpha = 0.25$, $r = 3$). If we choose the result produced by $F_e(v)$ of Fig. 5, we obtain a frequency $\omega \approx 0.74\omega_{e,1} \approx 1.5\Omega_{e,1}$, which is close to the result predicted by the dispersion relation.

5. Discussion

Present results clearly show that the microinstability observed in our simulations of perpendicular shock is a variety of the electron cyclotron drift instability which was studied in the 70's (see, e.g., Forslund et al., 1970; Gary, 1971,, and references in the review by Wu et al. 1984). It is a variety in the sense that the instability is not driven by the whole ions drifting as a bulk, yet just by an ion beam. Also, it takes place in the foot and propagates along the shock normal, while the electron cyclotron drift was thought to occur in the ramp and propagate parallel to the shock front. The latter turns out to be an important distinction. The various drifts that are caused by the gradients in x within the ramp and which occur in the y-direction were shown to detune the resonance condition leading to reduced growth rates (Gary, 1971). Here, since the wavevector is in the x-direction, the instability is unaffected by possible, gradient-related drifts in y.

A characteristic of the instability is its short wavelength. This may explain the difficulty to observe it either experimentally or in other previous numerical simulations of shocks. Because of the large wavenumber, the frequency that could be detected in the spacecraft frame is presumably significantly Doppler shifted from the electron gyrofrequency into some uncharacteristic frequencies. We should also emphasize that the instability may take place only for shocks with relatively cold ions, meaning where the ion thermal velocity is much less than the upstream shock velocity, for which self-reformation occurs. Moreover, then only a portion of the reformation cycle is concerned, as shown in Fig. 1.

Let us consider now what to expect when simulation parameters converge toward more realistic values. Using Eqs. (5), (6) and (2), one evaluates the relative drift between reflected ions and electrons as

$$U_{ri\text{–}e} \approx 2M_A\left(\frac{2}{\beta_e}\right)^{1/2}\left(\frac{m}{M}\right)^{1/2}(1-\alpha)(1-1/r)v_t. \qquad (10)$$

Now, a physical condition for the instability to occur is as follows. The electron cyclotron frequency of the first Bernstein wave needs to be seen by the reflected ions as close to a natural frequency of theirs. Therefore, one has the resonant condition

$$k(U_{ri\text{–}e} - v_{ti}) \approx \Omega_{e,f}, \qquad (11)$$

where the subscripts "e, f" denotes the electron cyclotron frequency evaluated in the foot. Combining Eqs. (10) and (11) where we assume v_{ti} to be negligible compared to $U_{ri\text{–}e}$, we obtain an estimate of the wavenumber in terms of simulation parameters:

$$k\lambda_d \approx \frac{1}{M_A}\left(\frac{M}{m}\right)^{1/2}\left(\frac{\Omega_e}{\omega_e}\right)\left(\frac{\beta_e}{2}\right)^{1/2}\left[\frac{r}{r-1}\,\frac{0.5}{(1-\alpha)}\,\frac{\Omega_{e,f}}{\Omega_{e,1}}\right]. \qquad (12)$$

The factor in square brackets is of order unity. For example, in our simulations we have $r \approx 3$, $\alpha \approx 0.25$ and $\Omega_{e,f}/\Omega_{e,1} \approx 1.5$, resulting in a factor 1.5. As discussed in Section 2.1 both factors M/m and ω_e/Ω_e, which are large numbers in the solar-terrestrial environment, have generally a fake reduced value in PIC simulations so as to decrease the computational effort and make the simulation altogether feasible. Raising the ion-to-electron mass ratio alone shortens the wavelength. Raising the ratio ω_e/Ω_e alone elongates the wavelength.

In order to test this prospective analysis, we performed two complementary simulation runs with a larger mass ratio, $M/m = 256$. For the first run all other parameters were kept the same. The cyclotron instability developed in the foot as described in this paper, yet with a wavelength of $9\lambda_{d,1}$, i.e. significantly shorter. Such a wavelength is at the limit of what our grid could resolve. For the second run, we also used $M/m = 256$, yet raised the plasma-to-gyro frequency ratio ω_e/Ω_e, while keeping the same β_e. The parameters were: $\Omega_{e,1}/\omega_{e,1} = 0.255$, $\beta_e = 0.034$ and $M_A = 3.0$. Again, the cyclotron instability emerged in the foot during the reformation cycle yet had now a wavelength of $19\lambda_{d,1}$. Thus, the unstable wavelength varied according to our expectations. Although this last run is preliminary and still needs to be analysed in detail, we show here the development of the instability as recorded. Fig. 7 displays profiles of the magnetic field B_z and the electrostatic field E_x for four successive snapshots. Again, a short-wavelength electrostatic instability emerges in the flat portion of the foot.

In light of the above, one should increase both M/m and ω_e/Ω_e when converging toward more realistic parameters. The two ratios compensate each other, making the electron cyclotron instability a promising candidate to account for the electrostatic turbulence in the shock front. Otherwise, if only M/m augments, the wavelength becomes so short that it is unphysical and/or invisible to the grid. The short wavelength combined

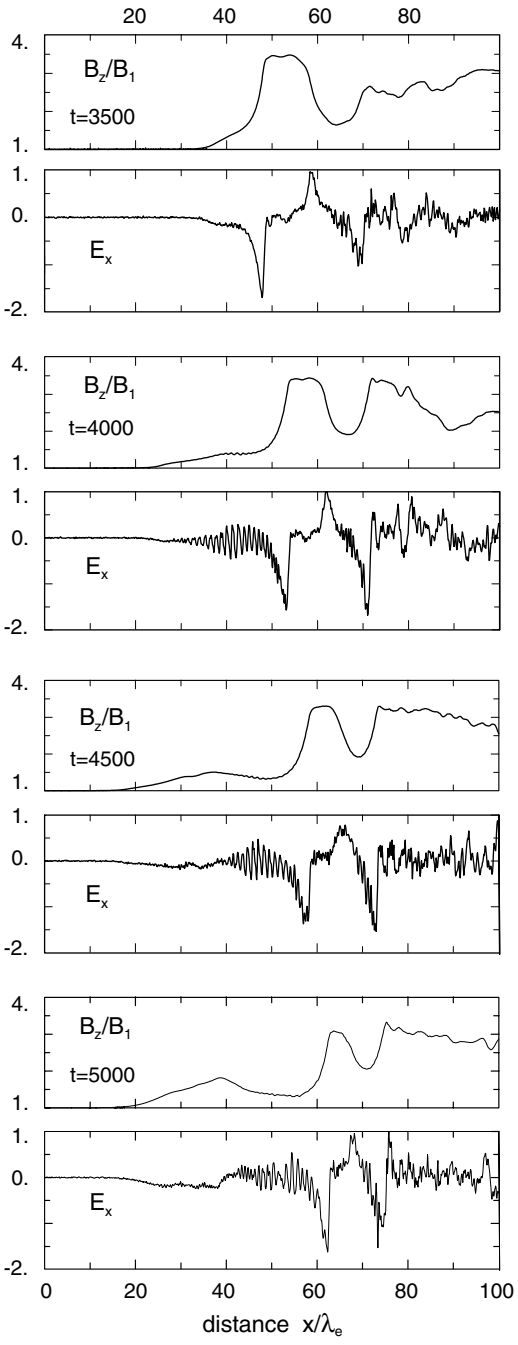

Fig. 7. Profiles of magnetic field B_z and electrostatic field E_x obtained in a run where both the ratio of masses and the ratio of plasma to gyro frequency are increased: $M/m = 256$ and $\omega_e/\Omega_e = 3.9$. A short-wavelength electrostatic instability emerges in the flat portion of the foot, as in Fig. 2. See discussion in the text.

with the parameter choice explains why this instability has not been observed in previous simulation works. Table 2 provides a comparison between different PIC simulations: chosen values of parameters and the associated wavenumber predicted by formula (12) are shown. Hada et al. (2003) with $k\delta = 1.5$ and Lembège and Savoini (1992) with $k\delta = 2.6$ clearly lack the grid resolution.

Table 2
Comparison of simulation regimes

Simulations	M_A	M/m	ω_e/Ω_e	λ_e/λ_d	$k\lambda_d$	$k\delta$
Present	3	100	2	15	0.3	0.6
Hada et al. (2003)	3	84	2	15	0.3	1.5
Lembège and Savoini (1992)	2.2	42	2	7	1.1	2.6
Scholer et al. (2003)	6	1836	2	9	1.2	0.6
Ideal	3	1836	50	200	0.2	N/A

Scholer et al. (2003) report a 90° case with real mass ratio $M/m = 1836$ and good grid resolution. At this point, why they did not see the instability is an open question which is under active investigation.

If we consider the cold limit, where the relative drift U_{ri-e} between reflected ions and electrons is much larger than the electron thermal spread, then both χ_e and χ_i greatly simplify. Taking the limit $\eta \to 0$ in Eq. (8) and $v_{ti} \to 0$ in Eq. (9) leads to the dispersion relation

$$1 + \frac{\omega_e^2}{\omega^2 - \Omega_e^2} + \frac{\alpha\omega_i^2}{(\omega - kV_{dr})^2} = 0. \tag{13}$$

The electron mode which the ion beam mode couples to is now the upper hybrid. Furthermore, for $\Omega_e \ll \omega_e$ one recovers the famous Buneman instability observed by Shimada and Hoshino (2000) in their simulations. We note also that when the Buneman instability is possible, its development is so fast that it preempts the slower cyclotron instability we have discussed here.

To close this section, we note that the microinstability does not strongly alter the global dynamics of the reflected ions. As visible in Fig. 4, their accumulation at the upstream end of the foot is still the main source of the shock front self-reformation. Even if the instability amplitude is quite large, the associated ion diffusion fills only partially the large "vortex" in phase space which forms in front of the ramp. The present case differs from the oblique, quasi-perpendicular situation studied by Scholer and Matsukiyo (2004). Their setup allows the modified two-stream instability to develop, which was seen to drastically alter the "vortex" pattern. In their case, the instability interacts with the incoming ions, which leads to their phase mixing with the reflected ions and to the formation of a new ramp upstream of that region of heated ions. We conclude that the difference is due to the electron cyclotron instability acting locally in phase space, only on the reflected ions and, moreover, only on a portion of their trajectory within the large scale "vortex".

6. Conclusion

By means of PIC simulations, we have shown that there is a microinstability in the foot of strictly perpendicular shocks that does not require a large relative drift

between reflected ions and the electron bulk. As such, it takes place for moderately supercritical shocks and emerges during the self-reformation phase, when a beam of reflected ions progresses upstream. The instability basically results from the coupling of electron Bernstein waves with an ion beam mode carried by the reflected ions. It is mainly electrostatic and propagates along the shock normal toward upstream as the ion beam. As its phase velocity is close to the beam velocity, it has a noticeable impact on both the populations of electrons and reflected ions, but does not interact with the incoming ions. Its wavelength is shorter than an electron inertia length and requires a fine grid to resolve, for which a Darwin-type PIC code reveals to be quite adapted. It is the first time this microinstability is observed in a truly self-consistent model, where the instability is embedded within the larger frame of an evolving shock structure. It could be a component of the electrostatic turbulence observed in the front of the terrestrial bow shock.

Acknowledgements

I (L.M.) thank Ilan Roth for several helpful discussions. I also gratefully acknowledge conversations with Stuart Bale and Art Hull, which have contributed to forming my understanding of shocks. The computations were performed on the IBM SP of the Supercomputer Center in San Diego. The research is supported by NASA with the Grants NNG04GF87G and NAG5-12989.

References

Biskamp, D., Welter, H. Ion heating in high-Mach number, oblique collisionless shock waves. Phys. Rev. Lett. 28, 410–413, 1972.

Forslund, D.W., Morse, R.L., Nielson, C.W. Electron cyclotron drift instability. Phys. Rev. Lett. 26, 1266–1270, 1970.

Gary, S.P. Longitudinal waves in a perpendicular collisionless plasma shock. J. Plasma Phys. 6, 561–566, 1971a.

Gary, S.P. Longitudinal waves in a perpendicular collisionless plasma shock. J. Plasma Phys. 7, 417–425, 1971b.

Hada, T., Oonishi, M., Lembège, B., Savoini, P. Shock front nonstationarity of supercritical perpendicular shocks. J. Geophys. Res. 108, 1233, 2003.

Hewett, D.W. Elimination of electromagnetic radiation in plasma simulation: the Darwin or magnetoinductive approximation. In: Ashour-Abdalla, M., Dutton, D.A. (Eds.), ISSS-2, Space Plasma Simulations. Reidel Publishing, Dordrecht, pp. 29–40, 1985.

Hoshino, M., Shimada, N. Nonthermal electrons at high Mach number shocks: electron shock surfing acceleration. Astrophys. J. 572, 880, 2002.

Lee, R.E., Chapman, S.C., Dendy, R.O. Numerical simulations of local shock reformation and ion acceleration in supernova remnants. Astrophys. J. 604, 187, 2004.

Lembège, B., Dawson, J.M. Self-consistent study of a perpendicular collisionless and nonresistive shock. Phys. Fluids 30, 1767–1788, 1987.

Lembège, B., Savoini, P. Nonstationarity of a two-dimensional quasiperpendicular supercritical collisionless shock by self-reformation. Phys. Fluids B 4, 3533–3548, 1992.

Leroy, M.M., Winske, D., Goodrich, C.C., et al. The structure of perpendicular bow shocks. J. Geophys. Res. 87, 5081–5094, 1982.

Matsukiyo, S., Scholer, M. Modified two-stream instability in the foot of high Mach number quasi-perpendicular shocks. J. Geophys. Res. 108 (A12), 1459–1468, 2003.

McBride, J.B., Ott, E. Electromagnetic and finite β_e effects on the modified two-stream instability. Phys. Lett. A 39, 363–364, 1972.

McBride, J.B., Ott, E., Boris, J.P., Orens, J.H. Theory and simulation of turbulent heating by the modified two-stream instability. Phys. Fluids 15, 2367–2383, 1972.

Scholer, M., Shinohara, I., Matsukiyo, S. Quasi-perpendicular shocks: length scale of the cross-shock potential, shock reformation, and implication for shock surfing. J. Geophys. Res. 108 (A1), 1014–1024, 2003.

Scholer, M., Matsukiyo, S. Nonstationarity of quasi-perpendicular shocks: a comparison of full particle simulations with different ion to electron mass ratio. Ann. Geophys. 22, 2345–2353, 2004.

Shimada, N., Hoshino, M. Strong electron acceleration at high Mach number shock waves: simulation of electron dynamics. Astrophys. J. 543, L67–L71, 2000.

Tidman, D.A., Krall, N.A. Shock Waves in Collisionless Plasmas. Wiley, New York, 1971, 175pp.

Wu, C.S., Winske, D., Zhou, Y.M., Tsai, S.T., Rodriguez, P., Tanaka, M., Papadopoulos, K., Akimoto, K., Lin, C.S., Leroy, M.M., Goodrich, C.C. Microinstabilities associated with a high Mach number, perpendicular bow shock. Space Science Reviews 37, 63–109, 1984.